Supporting information for: A small effective charge describes DNA–DNA interactions in tight supercoils

Cristopher Maffeo, Robert Schöpflin, Hergen Brutzer, René Stehr, Aleksei Aksimentiev,* Gero Wedemann,* and Ralf Seidel*

E-mail: aksiment@illinois.edu; gero.wedemann@fh-stralsund.de; ralf.seidel@biotec.tu-dresden.de

Supplementary Discussion - Effects from fluctuations

It is quite surprising that the model introduced in the main text, which *neglects fluctuations*, provides such an excellent description of the experimentally determined slopes and torques after buckling (see Figures 1c and 2, main text). Judging the success of the model by its agreement with the experimental data, one would conclude that it correctly covers the major determinants of superhelix formation under external tension. However, it is also clear that fluctuations should influence the measured parameters. Within this section we discuss the reasons for the success of our approach as well as its disadvantages and limitations.

Verification of the applied parameters. One possible explanation for the agreement of our theoretical approach with the experimental data is that the parameters which enter the formula for the superhelix formation energy $E_{\mathrm{tot}}^{\mathrm{sh}}$ (see eq 1, main text) were over- or underestimated, thereby compensating the error due to neglected fluctuations.

The only adjustable parameters entering our model are the persistence length p (for which a constant value of 50 nm is taken throughout the paper) and the DNA charge adaptation factor χ_{CR}.

*To whom correspondence should be addressed

Although the persistence length is expected to depend weakly on the ionic strength,[1] varying this parameter within a reasonable range[1] only leads to minor changes of χ_{CR} (changing p by 5 nm alters χ_{CR} only by ± 0.03). Thus, the salt dependence of the persistence length can be neglected within error.

To obtain verification for the charge adaptation factor χ_{CR}, we carried out coarse-grained Monte-Carlo (MC) simulations (see main text) that, by definition, include all fluctuation-based effects, such as undulation enhancement of the electrostatic interactions.[2] No additional entropic energy terms, e.g. due to DNA confinement within the plectoneme,[3] are required. The Hamiltonian for the MC simulations includes energy terms corresponding to those in the theoretical model with the same values for the parameters p and χ_{CR}. In addition, the MC simulations include the DNA twist energy, for which a torsional persistence length p_{tor} = 100 nm was taken.[4] While variations of p_{tor} change the buckling position in an approximately proportional fashion,[5] they do not impact the slope or torque after buckling. In fact buckling does occur slightly earlier in simulations than in experiments (compare Figures 1b and 3b, main text), but this can be adjusted in the simulations by applying a slightly reduced value for p_{tor} of 94 nm as recently reported.[6]

We verified that the electrostatic energies agree as calculated by the theoretical model and the MC simulations. In addition, the dependence of the superhelix energy on the superhelical radius ρ was found to agree when calculated using either approach (Figure S8). We can also exclude mistakes due to imprecise writhe estimates, since the twist is explicitly included for each segment in the MC simulations. Writhe calculations are only carried out to prevent MC moves in which strands would virtually cross each other and change the linking number (defined as twist plus writhe) by ± 2.

For χ_{CR} = 0.42 the slopes from the MC simulations are in excellent agreement with the ones predicted by the theoretical model (Figure 3c, main text). Therefore, χ_{CR} = 0.42 must be applied in order to describe the supercoiling data given the manner with which the electrostatic interactions are calculated.

Applying additional entropic energy terms. In previous theoretical work on supercoiled plas-

mid DNA, additional entropic energy terms have been included to model the effect of the confinement that DNA experiences within a tight plectonemic superhelix compared to the more freely fluctuating non-superhelical state. Marko & Siggia[3] considered the additional free energy per DNA length $E_{\mathrm{entr}}/L = k_{\mathrm{B}}T[p^{-1/3}(h/2)^{-2/3} + p^{-1/3}\rho^{-2/3}]$ to model confinement of the radial fluctuations within the superhelical radius ρ and pitch fluctuations within the superhelical repeat length h. Ubbink et al.[2] considered a similar confinement, where the radial fluctuations are limited to an adjustable confinement length d_{r} and the pitch fluctuations to $h/2\pi$ with $E_{\mathrm{entr}}/L = k_{\mathrm{B}}T \cdot 3/2^{8/3}[p^{-1/3}(h/2\pi)^{-2/3} + p^{-1/3}d_{\mathrm{r}}^{-2/3}]$. Additionally Ubbink et al. introduced a correction to the electrostatic interaction energy due to radial superhelix fluctuations leading to an enhancement factor of $\exp(2d_{\mathrm{r}}^2/\lambda_{\mathrm{D}}^2)$ compared to the interaction energy in the absence of fluctuations.

In order to better understand the role of fluctuations in particular the influence of confining the DNA within the superhelix, we applied the energetic corrections from both theoretical works within our theoretical model. While the slopes are well described for χ_{CR} = 0.45, the torques are overestimated considerably by the corrections from both theories (Figure S6). Plotting only the entropic contribution to the superhelix free energy reveals an approximately constant offset to the energy for all forces considered. Subtracting the energetic corrections for confinement and fluctuations provides torque values in close agreement with our theoretical model (Figure S7a). This is because the superhelix parameters hardly change when the additional corrections are applied (shown for ρ in Figure S7b).

From this we can formulate two conclusions: (i) including energetic penalties for confinement of the DNA within a tight superhelix does not lead to an increase of the superhelix dimensions and (ii) the actual free energy contributions of the fluctuations are considerably smaller than predicted for supercoiled plasmids. The latter is not surprising, since DNA under tension is already significantly confined before superhelix formation compared to relatively freely fluctuating non-superhelical, circular DNA. Additionally, extrusion of a superhelix, which can freely diffuse along and around the stretched part of the DNA, liberates some of the confinement of the stretched configuration. In our opinion this is the most likely reason for the relatively small entropic contributions

to the free energy of superhelix formation.

Though the predictions for supercoiled plasmids do not provide a correct quantification of the entropic contributions for DNA under tension, it is interesting to note that they seem to add a constant energetic offset for the range of forces considered. Comparing the torque predictions from our theoretical model with the torque from the MC simulations reveals a constant offset of $\sim$1.5 pN nm for all forces and salt concentrations (Figure 3e, main text), which is likely the aforementioned contribution due to fluctuations.

Fluctuations within stretched versus superhelical DNA - relative extension of DNA. An additional complication arises when considering the influence of fluctuations on DNA length changes. If one considers the average DNA path, i.e. the average over the DNA fluctuations in time, it appears to be always shorter than the contour length of the molecule. Thus, for DNA under tension, the end-to-end distance is always shorter than the contour length and the DNA can be considered as an entropic spring. Consequently, within a DNA supercoiling experiment, the plectonemic superhelix takes up more DNA per added turn than indicated by the slope of the supercoiling curve. To account for the additional DNA sequestered within the average DNA path, previous works[7,8] solved for superhelix parameters in the absence of fluctuations, as done here, and scaled the resultant slopes by the relative extension z_{rel} of the DNA at zero twist, defined as the end-to-end distance under the given tension divided by the contour length of the DNA.

This approach, however, ignores the strong dependence of z_{rel} on the DNA twist (which is particularly large at low forces). More importantly, only the average DNA path is rescaled but not the relevant energy terms which define the superhelix dimensions.

The superhelix energy should, however, be rescaled to account for the rescaling of the DNA geometry and the resulting rescaled energy should be minimized to produce a new set of superhelix parameters. When rescaling with z_{rel} as done before[7,8] one could assume that the fluctuations contributing to z_{rel} are suppressed within the superhelix (with $z_{\mathrm{rel}} = 1$ within the superhelix) so that only the potential energy imposed by the applied tension would need to be rescaled (i). Alternatively, all energy terms could be linearly rescaled by z_{rel} (ii). The first possibility would lead to

different superhelix parameters and therefore to a different slope prediction than previously determined,[7,8] whereas the second approach would provide slopes (as obtained before[7,8]) and torques, both rescaled by z_{rel}.

However, fluctuations do occur within the plectoneme, so $z_{\mathrm{rel}} = 1$ (assumption i) is not obeyed within the plectoneme. Also, the energies for the supercoiled DNA do not scale linearly with the superhelix dimensions (assumption ii). In particular, the electrostatic interactions do not decrease but rather increase in an approximately exponential fashion upon scaling the superhelix with z_{rel}. In agreement with these arguments, we find that neither approach of rescaling the superhelix energies with z_{rel} appropriately models the experimental data, since both bias the obtained slopes towards lower values (not shown). Matching the experimental data would require a significantly increased χ_{CR}, which contradicts the results from the MC simulations. Still, the dependence of the slopes on force would be poorly reproduced; adjusting χ_{CR} to obtain agreement for the slopes at elevated forces provides significant underestimation of the slopes at lower forces.

Why does our simple approach, which ignores fluctuations, work well?

One way of looking at this is to assume that the relative extension within the superhelix remains unchanged compared to the stretched DNA, i.e. that the bending fluctuations are not affected by the confinement of the DNA within the superhelix with z_{rel} being constant throughout the molecule. In this case, the superhelix from our theoretical model can be viewed as an effective path obtained after averaging out the fluctuations around it. The superhelical geometry and potential energy due to the applied tension would be correctly described; only the bending energy and the electrostatic interaction energy would change. We consider these changes to be minor, and in case of the electrostatic interactions even to cause a further reduction of χ_{CR}. Comprising more DNA, i.e. more charge, per average superhelical path length together with an enhancement of the effective electrostatic repulsion due to undulations[2] leads to an increased electrostatic contribution, which would need to be adjusted by lowering rather than increasing χ_{CR}. Thus, if assuming a constant z_{rel} throughout the molecule, our approach is expected to provide a reasonable description of the experimental slopes with minor adaptations for electrostatic and bending energies.

Another way of looking at the problem is to consider the asymmetry of the fluctuations of superhelix radius and pitch. Compared to the energetic minimum position, fluctuations that increase ρ and h are preferred over fluctuations which decrease these parameters due to the asymmetry of the energy landscape (shown for ρ in Figure S8), thereby increasing the slope (we note here that, judging from the energy landscape of the superhelix (not shown), correlated fluctuations of ρ and h are favored over anti-correlated ones). Indeed, at lower forces, we find that the mean superhelix radius obtained from MC simulations is shifted to higher values (Figure S7b) compared to the most probable radius, i.e. the energetic minimum position. However, we obtain excellent agreement between theory and MC simulation for the most probable radius (Figure S8). Thus to some extent, our model underestimates the mean superhelix dimensions by neglecting the asymmetry of fluctuations.

Taking the two viewpoints together:

(i) It is likely that confinement of the tightly wrapped DNA molecule partially suppresses bending fluctuations within the superhelix. This would increase z_{rel} within the superhelix and cause a *reduction of the slopes* as discussed above for the extreme suppression of the bending fluctuations, where $z_{\mathrm{rel}} = 1$ in the plectoneme was considered. (We note that such a slope reduction is partially compensated by the writhe originating from bending fluctuations,[9] which becomes liberated upon suppression of these fluctuations within the superhelix and needs additionally be accommodated.)

(ii) Global superhelix fluctuations favor larger averages for the superhelical parameters ρ and h (Figure S8), leading to a balancing *increase in the slopes*. The torque offset between our theoretical model and the MC simulations can then be viewed as the occupancy of less energetically favorable superhelix geometries due to ongoing fluctuations.

We therefore think that the striking agreement of our theoretical model with MC simulations and experimental data is due to opposing effects from the fluctuations - a reduced relative stretching within the superhelix versus fluctuations of the superhelix towards larger dimensions. Previous work ignored the latter part and failed to provide a quantitative description of the supercoiling slopes.[7,8] In any case our model provides a satisfactory way to calculate and predict slopes and

torques in supercoiling experiments under tension, which will be helpful for both future experimental[10] and theoretical work.[5,11]

Supplementary Methods

Coarse-grained Monte-Carlo simulations

Representation of the tethered DNA. DNA is represented as a linear chain of 129 straight segments with a length of 5 nm, which is significantly shorter than the bending and torsional persistence lengths (Figure S9a). Each segment is defined by its position and a local coordinate system, describing its spatial orientation. The elastic properties of the chain are described by standard harmonic potentials for stretching, bending and twisting.[12,13] The electrostatic interaction between DNA segments is described by a Debye-Hückel approximation adapted to fit the non-linear PB solution at large distances (see below and Figure S2). The DNA is attached to a 400 nm-radius sphere, that represents the magnetic bead on one end, and an infinite impenetrable plane on the other end (Figure S9b). Additional mechanical potentials were introduced to model the stretching of DNA by an external force, volume exclusion of any DNA segment from the bead and surface as well as tethering of the DNA chain at its extremities (see below). An overview of the used parameters is given in Table S1.

Table S1: Parameters used in the Monte-Carlo simulations. The values of the elastic potentials are based on experimentally determined values, corresponding to a 50 nm bending persistence length[14] and a torsional persistence length of 100 nm[4] and for elastic stretching to a stretching modulus of 1100 pN.[15]

Parameter	Value
Stretching modulus	$1.10 \cdot 10^{-18}$ J/nm
Bending modulus	$2.06 \cdot 10^{-19}$ J nm
Torsion modulus	$4.05 \cdot 10^{-19}$ J nm
Tether modulus (α_{tether})	$5.53 \cdot 10^{-19}$ J/nm^2
Intersection modulus (α_{IntSec})	$2.78 \cdot 10^{-7}$ J/nm^{12}
Temperature	293.0 K
Number of segments	129
Segment length	5 nm

Electrostatic Energy. The electrostatic interaction energy of the whole DNA chain was calculated by summing up the electrostatic interaction energy of individual segment pairs. Each pair entered

the sum only once. The electrostatic interaction between two individual DNA segments is determined in analogy to the calculations described in the main text (Eq. (4), main text, and Figure S2) by integrating the Poisson-Boltzmann adapted solution of the Debye-Hückel equation for a point charge over two charged line segments:[12]

$$E_{ij}^{\mathrm{Estat}} = l_{\mathrm{B}} \cdot k_{\mathrm{B}}T \cdot \xi^{*^2} \int ds_i \int ds_j \frac{\exp(-r_{ij}/\lambda_{\mathrm{D}})}{r_{ij}} \tag{S1}$$

The value l_{B} is the Bjerrum length in water, and λ_{D} the Debye length. $r_{ij} = r(s_i, s_j)$ is the distance between the current positions s_i s_j at the segments i and j. As described (see main text and Figure S2), the linear charge density $\xi^* = \xi \cdot \chi_{\mathrm{CR}} \cdot \chi_{\mathrm{Rod}} \cdot \chi_{\mathrm{PB}}$ is chosen such that the obtained potential coincides for large enough distances with the solution of the Poisson-Boltzmann equation for an infinite cylinder with charge density $\xi^* \chi_{\mathrm{CR}}$, with $\xi = 2\mathrm{e}/0.34$ nm. Unless indicated the factor χ_{CR} was set to 0.42 (see main text). To save computational time, the double integral of S1 was tabulated at the applied ionic strength prior to the simulations. The distance of the segments and three values describing the relative orientation of the segments to each other parameterize the table. During the simulation a linear interpolation of the tabulated values was used.

Potential, tethering and volume exclusion energies. For the simulation of DNA under tension and torsion, additional energy terms were introduced. The stretching was implemented by an energy E_{pull}:

$$E_{\mathrm{pull}} = \alpha_{\mathrm{tether}} \cdot d^2 - F \cdot z \tag{S2}$$

The first term of the equation tethers the DNA to the attachment plane and the magnetic bead, with d being the displacement of the first segment with respect to its origin. The strength with which the DNA chain was held at the tether point was determined by the parameter α_{tether} (see Tab. Table S1). The second term of the equation represents the potential energy of the DNA chain in the presence of the external pulling force F, where z is the distance between the last DNA segment and the attachment plane.

To fix the twist in the DNA, two additional segments with a fixed local coordinate system were placed in front of the first and behind the last DNA segment (Figure S9a). These two segments were only considered regarding their contributions to bending and twisting energy.

Chain movements were restricted by an impenetrable, infinite plane and a spherical excluded volume, modeling the cover slip of the flow cell and the magnetic bead, respectively, (Figure S9b). Both exclusions were realized by soft core potentials. The energetic penalty E_{IntSec} for a DNA-segment intersecting either bead or surface plane was calculated from its penetration depth p and a scaling factor:

$$E_{\mathrm{IntSec}} = \alpha_{\mathrm{IntSec}} \cdot p^{12} \tag{S3}$$

Knots and Writhe. The MC procedure allows segments to cross one another during simulation steps, which can cause knotted configurations[16] or change the number of turns initially added to the chain, i.e. the linking number Lk of the chain. To exclude such non-physical steps, the linking number was checked periodically using the condition $Lk = Tw + Wr$, where Tw is the twist and Wr the writhe of the DNA chain. The total twist can easily be derived by summing up the twist for each pair of adjacent segments. The writhe was computed according to ref. 17. Since the writhe is only defined for circular structures, the linear chain was closed virtually[16] (Figure S9c). Due to numerical errors the linking number fluctuated slightly ($\pm$ 0.1 turns). However, if the linking number differed more than a threshold of 0.5 from its nominal value, the obtained DNA configuration was rejected. Similarly, if a knot was detected using an algorithm described in ref. 18, the obtained configuration was rejected, too.

Simulation procedure. An ensemble of configurations which represents the thermal equilibrium distribution was generated with pivot, rotation,[19,20] crank shaft[16,21] moves and segment length variation.[22] The simulations were carried out at a temperature of 293.0 K. An overview of the simulation parameters is given in Table S1.

To calculate the number of uncorrelated configurations, the correlation times were determined from the autocorrelation function as described in ref. 13. The autocorrelation function was calculated for the energy, the average twist between adjacent DNA segments and the z-position of the

middle segment. The maximum autocorrelation time was calculated for different configurations. The maximal correlation time measured was $4.7 \cdot 10^4$ MC steps. Configurations separated by more than two times the correlation time can be considered as statistically independent.[23] Therefore, only configurations obtained every 10^5 MC steps were considered in our analysis. Additionally, the first 200 statistically independent configurations were not included in our analysis to avoid a bias towards the start structure. Every simulation run was carried out at least four times, each with $6 \cdot 10^7$ MC steps, to verify the results. Thus, overall a set of 1600 uncorrelated configurations was obtained for each combination of salt concentration, applied turns and pulling force used in the simulations.

Analyzing the MC-ensembles. According to the experimental results we derived several parameters from the statistically independent ensemble of DNA-configurations. In particular, we computed the average z-distance of the last segment of the chain, which was attached to the magnetic bead, as well as the average twist angle between adjacent DNA-segments from which the torque within the chain was calculated.

For a detailed analysis of the geometry of the plectonemic superhelix, we implemented a plectoneme-detecting algorithm as described in ref. 24 and labeled every segment that was a part of a superhelix. The distance of each segment in the plectoneme to the opposite strand was obtained to determine the distribution of the superhelix radius.

Simulation Software. The used simulation software was written in C++ and has been successfully used in several studies.[13,25–27] The algorithms were verified with an extensive set of unit tests and tests using simplified chain models with stretching modulus only and with additional bending and torsion energies, which reproduced the expected analytical values. In addition to run-time checks and automated unit tests, Rational Purify for Linux was used as a dynamic code analysis tool for error checks. Computations were performed on a Linux cluster (Quad Core AMD Opteron, 2.2 GHz) and on the parallel supercomputer at the North German Supercomputing Alliance (HLRN). A single simulation with $6 \cdot 10^7$ MC steps on a single processor core took between

7 h and 28 h, depending on the frequency in which invalid configurations were produced by Monte-Carlo moves (see section Knots and Writhe).

All-atom MD simulations

All MD simulations were performed using the program NAMD,[28] the parmbsc0 refinement of the AMBER parm99 force field,[29,30] the TIP3P water model,[31] standard parameters for ions,[32] periodic boundary conditions, and 1–2–4-fs multiple time stepping.[33] Van der Waals and short-range electrostatic potentials were calculated using a smooth (10–12 Å) cutoff; the particle mesh Ewald method was used to compute long-range electrostatics using a 1.0 Å-spaced grid. The temperature was kept constant by applying Langevin forces[34] to all non-hydrogen atoms; the Langevin damping constant was set to 0.1 ps^{-1}. Simulations were performed in the NPT ensemble using Nosé-Hoover Langevin piston pressure control[35] at 1 bar.

To find the ion distribution around double-stranded DNA, a two-turn poly(A·T) molecule was immersed in NaCl electrolyte. The DNA was placed so that its helical axis coincided with the z-axis of the simulation cell. Bonds were placed across the periodic boundary to make an effectively infinite DNA molecule. Hexagonal boundary conditions were employed in the xy-plane with 40 Å between periodic images for systems containing 1000, 320, or 170 mM electrolyte, and 85 Å for systems containing 60 or 30 mM electrolyte.

The method used to obtain the force between parallel double-stranded DNA molecules is described in the main text.

References

(1) Baumann, C. G.; Smith, S. B.; Bloomfield, V. A.; Bustamante, C. *Proc. Natl. Acad. Sci. USA* **1997**, *94*, 6185–6190.

(2) Ubbink, J.; Odijk, T. *Biophys. J.* **1999**, *76*, 2502–2519.

(3) Marko,; Siggia, *Phys. Rev. E* **1995**, *52*, 2912–2938.

(4) Bryant, Z.; Stone, M. D.; Gore, J.; Smith, S. B.; Cozzarelli, N. R.; Bustamante, C. *Nature.* **2003**, *424*, 338–341.

(5) Brutzer, H.; Luzzietti, N.; Klaue, D.; Seidel, R. *Biophys J.* **2010**, *98*, 1267–1276.

(6) Mosconi, F.; Allemand, J. F.; Bensimon, D.; Croquette, V. *Phys. Rev. Lett.* **2009**, *102*, 078301.

(7) Neukirch, S. *Phys. Rev. Lett.* **2004**, *93*, 198107.

(8) Clauvelin, N.; Audoly, B.; Neukirch, S. *Biophys. J.* **2009**, *96*, 3716–3723.

(9) Moroz, J. D.; Nelson, P. *Proc. Natl. Acad. Sci. USA*. **1997**, *94*, 14418–14422.

(10) Koster, D. A.; Croquette, V.; Dekker, C.; Shuman, S.; Dekker, N. H. *Nature* **2005**, *434*, 671–674.

(11) Daniels, B. C.; Forth, S.; Sheinin, M. Y.; Wang, M. D.; Sethna, J. P. *Phys. Rev. E* **2009**, *80*, 040901.

(12) Klenin, K.; Merlitz, H.; Langowski, J. *Biophys. J.* **1998**, *74*, 780–788.

(13) Wedemann, G.; Langowski, J. *Biophys J.* **2002**, *82*, 2847–2859.

(14) Bloomfield, V. A.; Crothers, D. M.; Tinocco, I. *Nucleic Acids Structures, Properties, and Functions*; University Science Books, 2000.

(15) Smith, S. B.; Cui, Y.; Bustamante, C. *Science* **1996**, *271*, 795–9.

(16) Vologodskii, A. V.; Marko, J. F. *Biophys. J.* **1997**, *73*, 123–132.

(17) Klenin, K.; Langowski, J. *Biopolymers* **2000**, *54*, 307–317.

(18) Khatib, F.; Weirauch, M. T.; Rohl, C. A. *Bioinformatics* **2006**, *22*, e252–e259.

(19) Metropolis, N.; Rosenbluth, A. W.; Rosenbluth, M. N.; Teller, A. H. *J. Chem. Phys.* **1953**, *21*, 1087–1092.

(20) Baumgärtner, A.; Binder, K. *J. Chem. Phys.* **1979**, *71*, 2541–2545.

(21) Arya, G.; Schlick, T. *J. Chem. Phys.* **2007**, *126*, 044107.

(22) Binder, K. *Monte Carlo and Molecular Dynamics Simulations in Polymer Science*; Oxford University Press, 1995.

(23) Sokal, A. D. Monte Carlo methods in statistical mechanics: foundations and new algorithms. *Functional Integration: Basics and Applications. Proceedings of the NATO ASI B-361*, Cargese (France), 1996.

(24) Wedemann, G.; Münkel, C.; Schöppe, G.; Langowski, J. *Phys. Rev. E* **1998**, *58*, 3537.

(25) Stehr, R.; Kepper, N.; Rippe, K.; Wedemann, G. *Biophys. J.* **2008**, *95*, 3677–3691.

(26) Kepper, N.; Foethke, D.; Stehr, R.; Wedemann, G.; Rippe, K. *Biophys. J.* **2008**, *95*, 3692–3705.

(27) Stehr, R.; Schöpflin, R.; Ettig, R.; Kepper, N.; Rippe, K.; Wedemann, G. *Biophys. J.* **2010**, *95*, in press.

(28) Phillips, J. C.; Braun, R.; Wang, W.; Gumbart, J.; Tajkhorshid, E.; Villa, E.; Chipot, C.; Skeel, R. D.; Kalé, L.; Schulten, K. *J. Comput. Chem.* **2005**, *26*, 1781–1802.

(29) Perez, A.; Marchan, I.; Svozil, D.; Sponer, J.; Cheatham, T. E.; Laughton, C. A.; Orozco, M. *Biophys. J.* **2007**, *92*, 3817–3829.

(30) Cheatham, T. E. I.; Cieplak, P.; Kollman, P. A. *J. Biomol. Struct. Dyn.* **1999**, *16*, 845.

(31) Jorgensen, W. L.; Chandrasekhar, J.; Madura, J. D.; Impey, R. W.; Klein, M. L. *J. Chem. Phys.* **1983**, *79*, 926–935.

(32) Beglov, D.; Roux, B. *J. Chem. Phys.* **1994**, *100*, 9050–9063.

(33) Batcho, P. F.; Case, D. A.; Schlick, T. *J. Chem. Phys.* **2001**, *115*, 4003–4018.

(34) Brünger, A. T. *X-PLOR, Version 3.1: A System for X-ray Crystallography and NMR*; The Howard Hughes Medical Institute and Department of Molecular Biophysics and Biochemistry, Yale University, 1992.

(35) Martyna, G. J.; Tobias, D. J.; Klein, M. L. *J. Chem. Phys.* **1994**, *101*, 4177–4189.

(36) Marko, J. F. *Phys. Rev. E* **2007**, *76*, 021926.

(37) Forth, S.; Deufel, C.; Sheinin, M. Y.; Daniels, B.; Sethna, J. P.; Wang, M. D. *Phys. Rev. Lett.* **2008**, *100*, 148301.

(38) Stigter, D. *J. Colloid Interf. Sci.* **1975**, *53*, 296–306.

(39) Harries, D. *Langmuir* **1998**, *14*, 3149–3152.

(40) Hammermann, M.; Steinmaier, C.; Merlitz, H.; Kapp, U.; Waldeck, W.; Chirico, G.; Langowski, J. *Biophys. J.* **1997**, *73*, 2674–2687.

Supplementary Figures

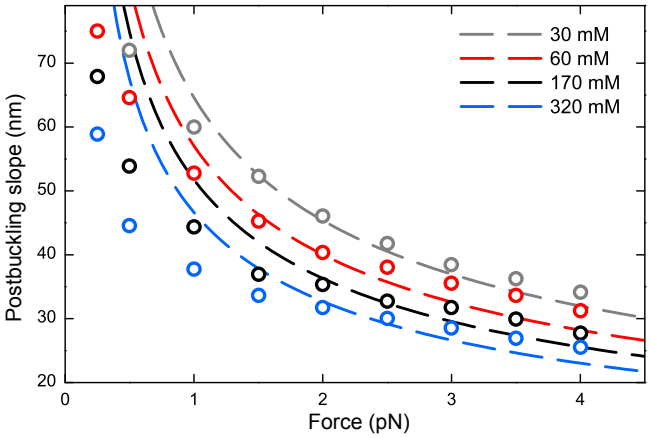

Figure S1: Comparison of the experimental slopes from the supercoiling curves with theoretical predictions after ref. 36. Experimental slopes (open circles) were taken from Figure 1 (main text). Theoretical predictions (dashed lines) were calculated as described[36,37] for empirically determined values of the plectonemic twist stiffness of 31, 28, 24, and 21 nm, to approximate the measured slopes at 30, 60, 170 and 320 mM Na^+, respectively. Particularly at elevated ionic strength, the theoretical prediction fails to correctly reproduce the force dependence of the measured slopes correctly.[6]

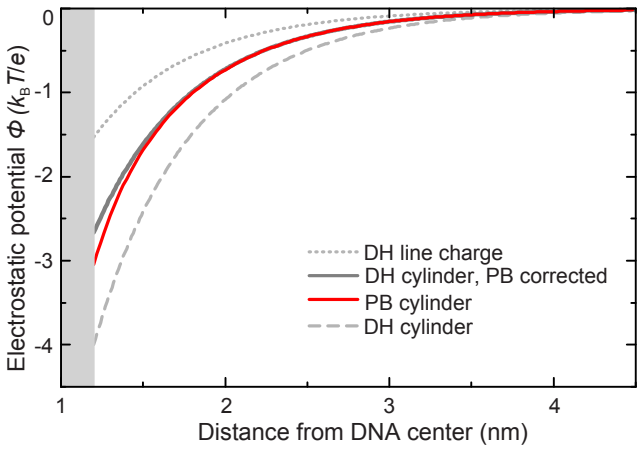

Figure S2: Electrostatic potential around a charged cylinder as applied within our theory compared to a full Poisson-Boltzmann (PB) solution. Potentials were calculated for a homogeneously charged cylinder with radius a = 1.2 nm and line charge density $\chi_{CR} \cdot \xi$ at 170 mM monovalent ions, where the adjustable charge adaptation factor $\chi_{CR} = 1.0$ and the nominal DNA charge density ξ = 2e/0.34 nm. A converging numerical solution for the electrostatic potential to the nonlinear PB equation (red line) was obtained using the COMSOL Multiphysics package (COMSOL, Inc.) in a one-dimensional geometry. The solution of the linearized PB, i.e. the Debye-Hückel (DH), equation for a charged, straight line with the same charge density (gray dotted line) was obtained by $\Phi = k_B T \cdot l_B \cdot \chi_{CR} \cdot \xi \int_s \exp[-r(s)/\lambda_D]/r(s) \cdot ds$ in analogy to Eq. (4) (main text). The solution of the DH equation for the cylindrical geometry (dashed gray line) is obtained the same way by multiplying ξ with χ_{Rod}, a geometry compensating factor; $\chi_{Rod} = \lambda_D/[a \cdot K_1(a/\lambda_D)]$, where K_1 is the 1st order modified Bessel function of the second kind. Due to the high DNA charge density the solution of the DH equation deviates significantly from that of the PB equation. Therefore, the DH solution was adapted by multiplication with another charge adaptation factor χ_{PB} to fit the PB solution for large distances (solid gray line). Values for χ_{PB} were taken from Stigter.[38] The final adapted line charge ξ^* density results then to $\xi^* = \xi \cdot \chi_{CR} \cdot \chi_{Rod} \cdot \chi_{PB}$. The obtained potential is in good agreement with the full solution of the PB equation with minor deviations close to the cylinder surface. Since χ_{PB} approximates 1 for low charge densities, the deviations shown in the figure for $\chi_{CR} = 1$ become even smaller for $\chi_{CR} = 0.42$. The cylinder boundaries are represented by a gray box.

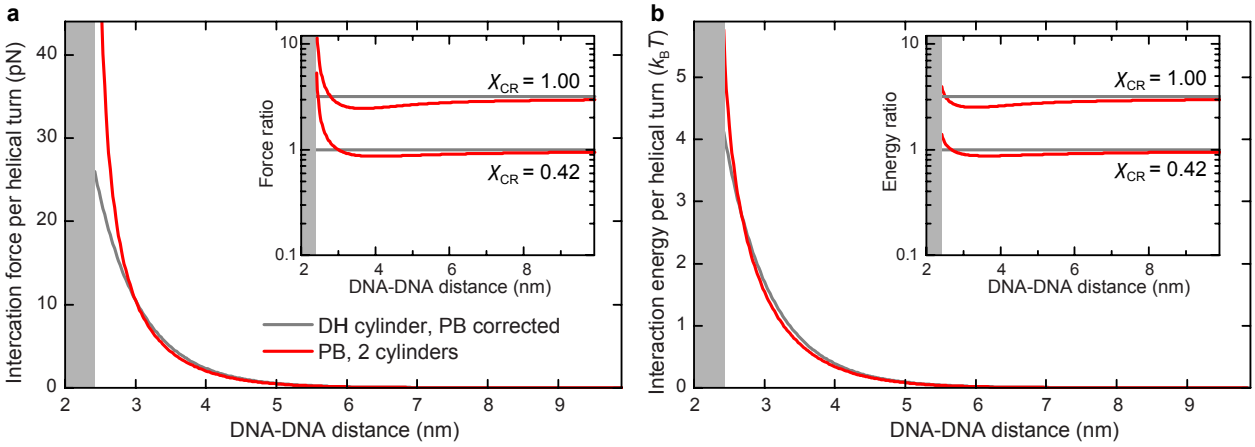

Figure S3: Interaction forces and energies between two charged cylinders as calculated within our theory compared to full Poisson-Boltzmann solutions. Interaction forces (in a) and interaction energies (in b) were calculated for two parallel homogeneously charged cylinders with radius a =1.2 nm at 170 mM monovalent ions and for a DNA line charge densities of $\chi_{CR} \cdot \xi$ with ξ = 2 e/0.34 nm and χ_{CR} = 0.42. Curves obtained from full PB solutions are shown as red lines. The gray box denotes the DNA-DNA distances at which the two cylinders would intersect each other. Simplified calculations as applied in our theory are shown as gray lines. Numerical solutions for the electrostatic potential of the nonlinear PB equation in a bicylindrical coordinate system were obtained as described[39] using the COMSOL Multiphysics package (COMSOL, Inc.). The obtained potentials were then used to calculate the interaction forces and energies within the PB formalism.[39] Approximate interaction energies as applied within our theory using adapted DH solutions that approach the PB solutions for large distances (see Figure S2) were calculated according to Eq. (4) (main text). A more detailed description of the charge adaptation parameters is given in Figure S2. Interaction forces were obtained by differentiating the interaction energies with respect to the DNA-DNA distance. The insets depict the ratios of the interaction forces and energies obtained from full PB solutions and adapted DH solutions for values of χ_{CR} of 0.42 and 1.0 with respect to the values from the adapted DH solution with χ_{CR} = 0.42. Deviations of the simplified calculations from the full PB treatment are small (<10% for χ_{CR} = 0.42 for DNA-DNA distances larger than 3 nm) compared to changing χ_{CR} from 1.0 to 0.42 (more than 3-fold change) except for small distances where the cylinders almost touch each other. The stronger repulsion at short distances found for the PB solutions can not explain the small effective charge used to describe the supercoiling data, since the interactions calculated from the adopted DH solutions already underestimate the interaction from the PB solutions, which would thus correspond to an even smaller effective value of χ_{CR}.

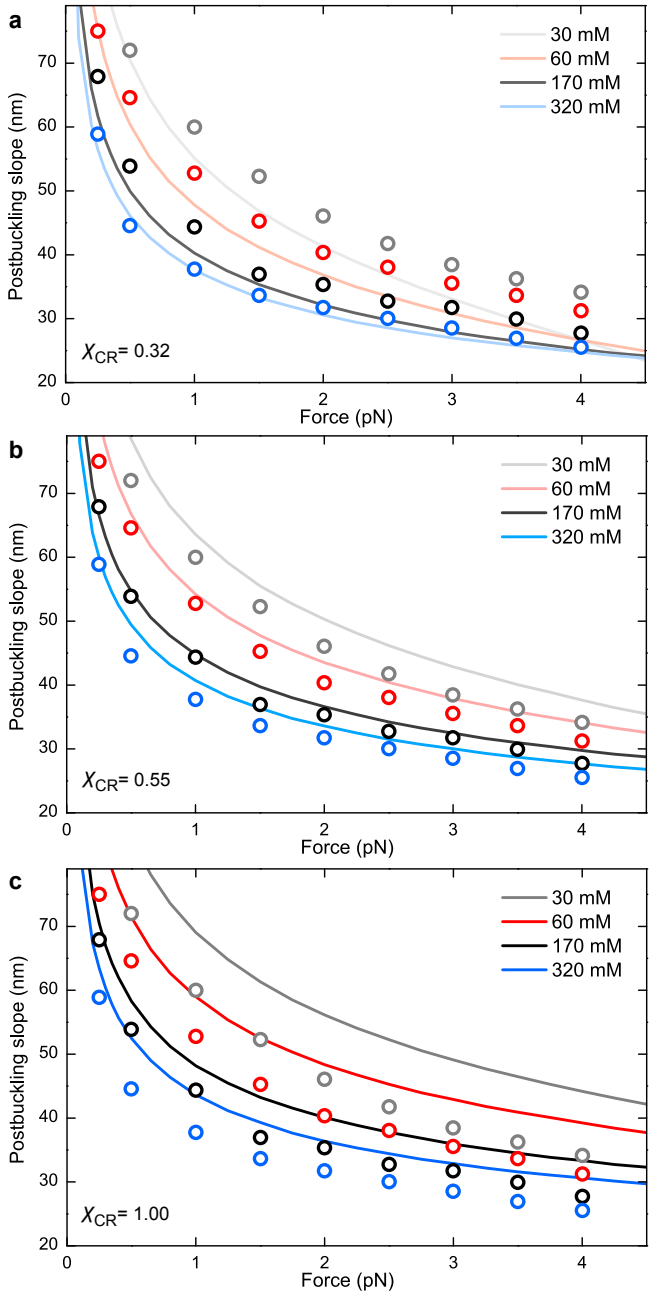

Figure S4: Comparison of experimental slopes from supercoiling curves with predictions of our theoretical model for different values of the charge adaptation factor χ_{CR}. Experimental slopes from Figure 1 are shown as open circles. Theoretical predictions for (a) $\chi_{CR} = 0.32$, (b) $\chi_{CR} = 0.55$ and (c) $\chi_{CR} = 1.00$ are shown as solid lines. Gray, red, black and blue colors indicated values obtained for Na^+ concentrations of 30, 60, 170 and 320 mM, respectively. Note that changing χ_{CR} from its optimum value of $\chi_{CR} = 0.42$ (see Figure 1c, main text), leads to a global under- or overestimation of the slopes at all salt concentrations. These deviations occur most prominently at higher forces, i.e. for small superhelix radii (Figure S7). They are relatively less pronounced (see also Figures 1b and 3c, main text) at low forces ($\leq$ 1 pN), i.e. larger superhelix radii. This likely explains why previous theoretical work[2,3] and MC simulations[12,40] describing the configurations of supercoiled plasmid DNA with larger superhelix radii were less sensitive to the correct choice of χ_{CR}.

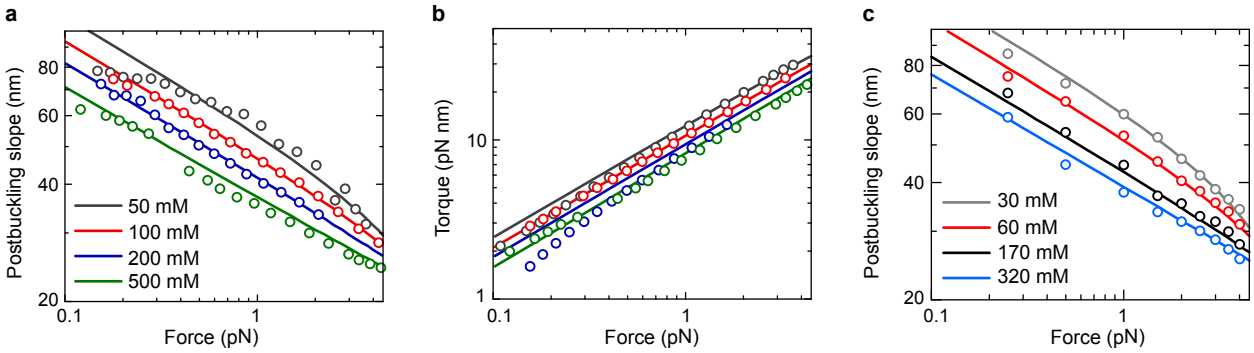

Figure S5: Double-logarithmic plots of experimentally obtained slopes and torques after buckling compared to theoretical predictions with $\chi_{CR} = 0.42$. The plots shown correspond to Figures 2a, 2b and 1c. Experimental data in (a) and (b) was taken from ref. 6. Experimental data in (c) is from the present study. The double-logarithmic plots demonstrate that our theoretical model accurately describes the scaling of slopes and torques with the applied force. The slopes at elevated ionic strength and the torques at all ionic strength approximately scale with a power law.[6]

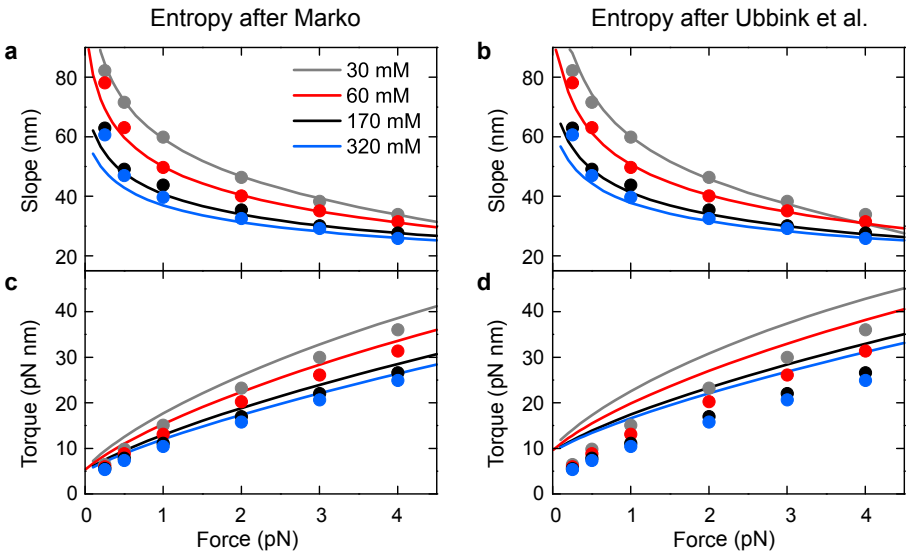

Figure S6: Model predictions including fluctuations. (a,c) Slopes, torques after buckling from coarse-grained Monte-Carlo simulations together with theoretical predictions that include an entropic energy term after Marko & Siggia[3] (see Supplementary discussion). (b,d) Slopes, torques after buckling from coarse-grained Monte-Carlo simulations together with theoretical predictions that include an entropic energy term and electrostatic undulation enhancement after Ubbink et al.[2] (see Supplementary discussion). Data from Monte-Carlo simulations is shown as filled circles, theoretical predictions as solid lines. For both models $\chi_{CR} = 0.45$ was taken, for which best agreement of the slopes was obtained.

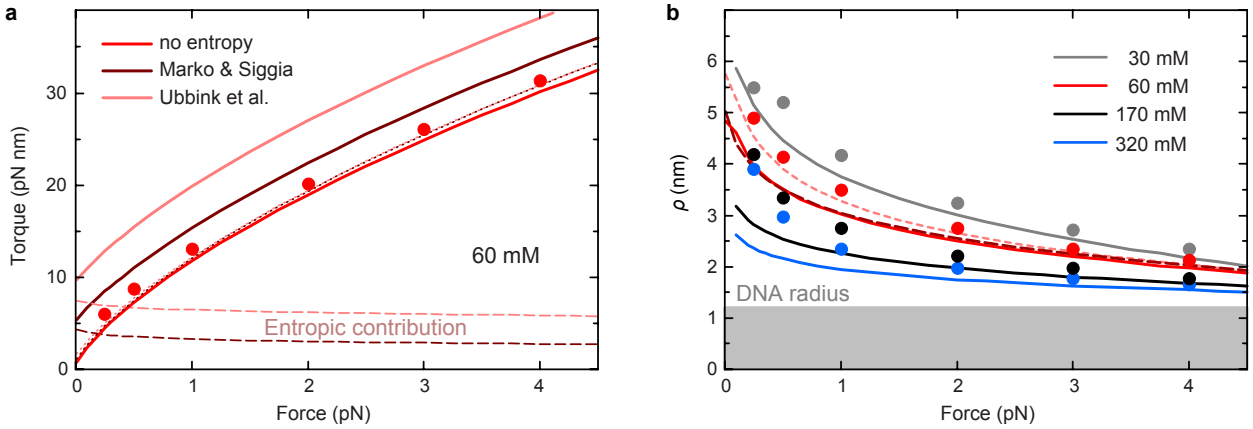

Figure S7: Entropic contributions to superhelix formation. (a) Torque after buckling at 60 mM Na^+ from coarse-grained Monte-Carlo simulations (red circles) together with predictions (solid lines) from the theoretical model (see main text), which neglects entropy, and alternative models (see Supplementary discussion) including entropic terms after Marko & Siggia[3] (brown line) and Ubbink et al.[2] (rose line). Dashed lines represent the entropic contributions to the torque. Dotted lines are obtained from the total predicted torque after subtracting the entropic contributions from the alternative models as well as the electrostatic undulation enhancement of about 2 pN nm (not shown) from the model of Ubbink et al. Predictions were calculated using $\chi_{CR} = 0.42$ for the model excluding entropy and $\chi_{CR} = 0.45$ for the models including entropy. (b) Mean superhelical radius ρ for different salt concentrations obtained from coarse-grained Monte-Carlo simulations (circles) and predictions from the model excluding entropy (solid lines). For 60 mM Na^+ also the predictions for the two models including entropy are shown (dashed lines, colors as in a).

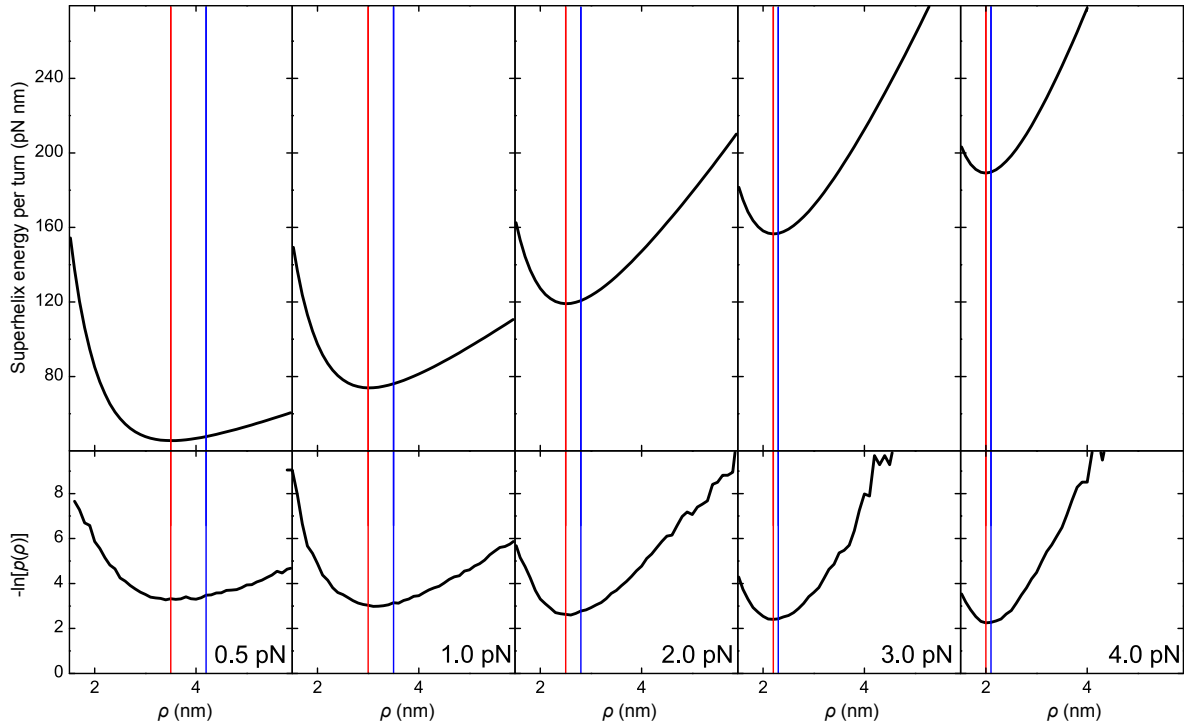

Figure S8: Fluctuations of the superhelical radius ρ as function of force at 60 mM monovalent ions. (*Top*) Dependence of the superhelix formation energy $E_{\mathrm{tot}}^{\mathrm{sh}}$ on ρ around the energy minimum position at constant superhelical pitch h as calculated from the theoretical model (see Eq. (1) main text). (*Bottom*) Negative natural logarithm of the probability distribution for the superhelical radius ρ obtained from coarse-grained Monte-Carlo simulations. It corresponds in arbitrary units to the energy to form a superhelix with radius ρ albeit with non-constant h. While the shapes of the energy distributions along ρ as well as the energy minimum positions (red lines) of the theoretical model and the simulations are in good agreement, the mean superhelical radius from the simulations (blue line) is shifted to higher values compared to the position of the energy minimum. This is most pronounced at lower forces. Due to the asymmetry of the energy distribution, deviations of ρ from the minimum position towards higher values are preferred over deviations towards lower values. The good agreement between the shapes of the energy distributions from theory and simulations serves as an independent validation that equivalent energy terms have been used in both approaches .

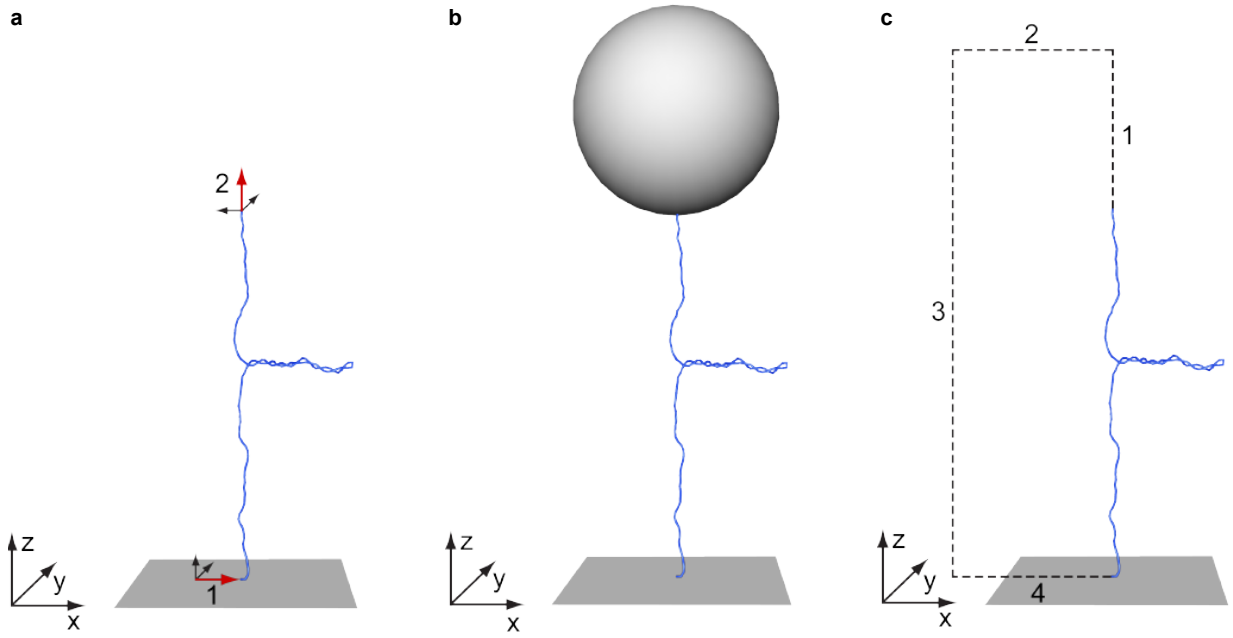

Figure S9: Representation of the tethered DNA within the coarse-grained MC simulations. (a) The DNA is represented as a linear chain of 129 straight segments, each with a length of 5 nm. To achieve torsional constriction, two additional segments (indicated as red arrows) with a fixed local coordinate system were introduced at each end of the chain. For these segments only energetic contributions due to bending and twisting were considered. (b) The chain is sterically restricted by an impenetrable infinite surface and the magnetic bead (bead is not to scale, the bead radius was 400 nm in the simulations). Volume exclusion was achieved by applying soft core potentials (see Supplementary Methods). (c) For the computation of writhe, the chain was virtually closed (image not to scale). The chain was extended at each end with the additional segments 1 and 4, each having the length of the DNA contour. These two long segments were connected with the perpendicular segments 2 and 3 in order to close the chain.

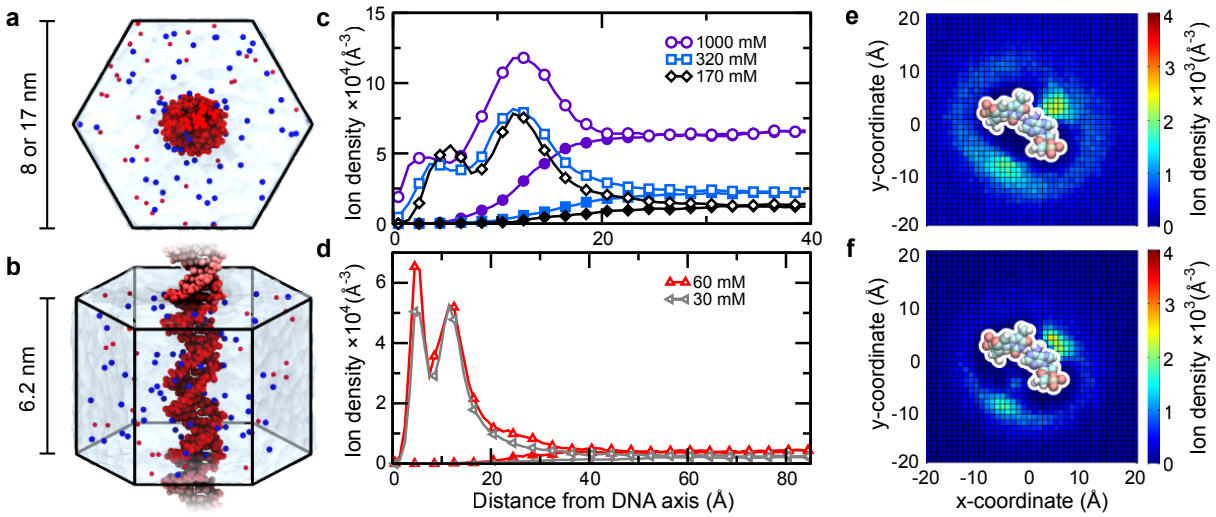

Figure S10: The distribution of monovalent ions around double-stranded DNA. (a,b) All-atom model used to find the ion distribution around DNA in MD simulations. The DNA atoms are depicted as red spheres; the counter and co ions are depicted as blue and red spheres, respectively; the water is shown as a semi-transparent molecular surface. (c,d) The radial ion distribution around DNA. Counter-ion (open symbols) and co-ion (filled symbols) distributions are shown for 1000, 320, 170 (c), 60, and 30 (d) mM NaCl concentrations. (e,f) The 2D counter-ion density around DNA. A z-dependent rotation was applied in the xy-plane to counter the helical pitch of canonical DNA; the counter-ion density was subsequently averaged along the z-axis. Data is shown for 320 (e) and 30 (f) mM bulk ion concentrations. A typical basepair is shown after the transformation was applied, indicating the approximate position of the DNA. The transformation has the effect of radially smearing the ion distribution, making it appear as though the ion concentration near the adenine is larger than that near the DNA phosphates (which are located further from the origin). In actuality, more counter ions can be found in close proximity of a DNA phosphate than an adenine at a given time.

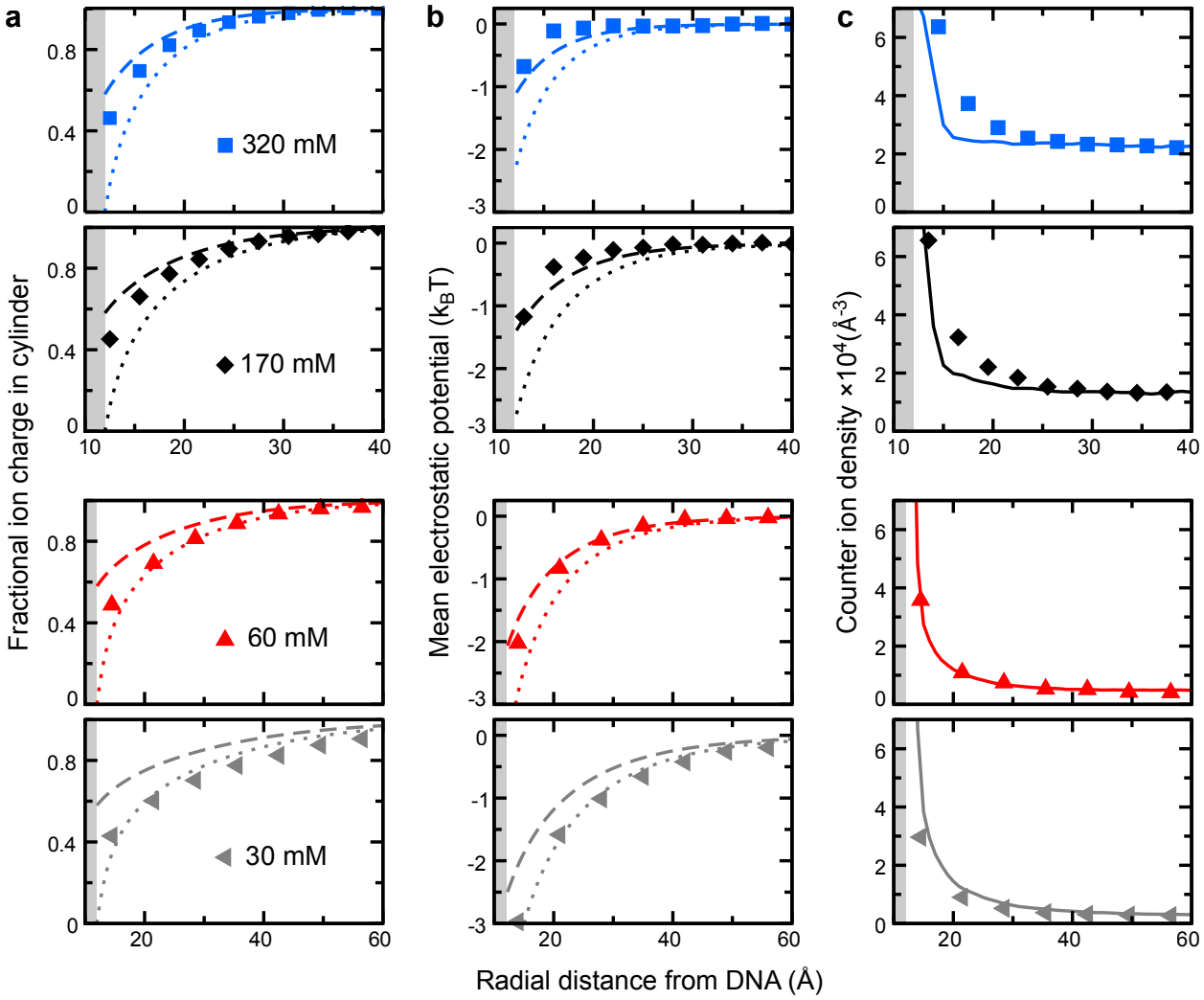

Figure S11: Charge distribution and potential around double-stranded DNA. Data resulting from MD simulations described in Figure S10 are plotted as solid symbols. Solutions to the non-linear Poisson-Boltzmann equation for a cylinder of 1.2 nm radius within a hexagonal unit cell (of same size as used in the simulations) are shown for $\chi_{CR} = 1.0$ (dotted lines) and $\chi_{CR} = 0.42$ (dashed lines) at each ion concentration. The cylinder boundary is represented by a gray box. (a) The fraction of the total ionic charge contained within virtual cylinders of increasing radii around the DNA nearly matches the PB solution for $\chi_{CR} = 1.0$ at low ion concentration. At higher ion concentration, the enclosed charge is somewhere between the PB predictions for $\chi_{CR} = 0.42$ and $\chi_{CR} = 1.0$. (b) The mean electrostatic potential around the DNA similarly matches the prediction for $\chi_{CR} = 1.0$ at low ion concentration, but falls to zero even more rapidly than predicted with $\chi_{CR} = 0.42$ at high ion concentration. The instantaneous 3D electrostatic potential was calculated by averaging over the trajectory in 5 ps intervals. Subsequently the z-axis and azimuthal angles were averaged out to obtain the data shown. Using Boltzmann weights to perform the spatial average was found to affect the results only very weakly. (c) Comparing the counter ion distribution expected from a Boltzmann weight of the potential from the MD simulations in b (solid line) to the directly observed counter ion density (symbols) reveals that the mean electrostatics fails to describe the counter ion density at high ion concentration.